PAPER

Check for updates

Fast Mg-ion insertion kinetics in V$_2$Se$_9$†

Matthew A. Wright, [ID] [abc] Jungwoo Lim, [ID] [ab] Raul A. Pacheco Muino,[a] Anna E. Krowitz, [ID] [a] Cara J. Hawkins, [ID] [a] Mounib Bahri, [ID] [dg] Luke M. Daniels,[a] Ruiyong Chen, [ID] [a] Luciana Gomes Chagas,[e] James Cookson,[e] Paul Collier,[e] Alan V. Chadwick,[f] Nigel D. Browning,[dg] John B. Claridge,[a] Laurence J. Hardwick [ID] *[ab] and Matthew J. Rosseinsky [ID] *[a]

V$_2$Se$_9$ displays facile electrochemical insertion of up to 1.6 Mg^{2+} per unit formula with fast diffusion (coefficients of 10^{-10}–10^{-12} cm^2 s^{-1}) surpassing best-in-class materials like Mo$_6$S$_8$. Detailed structural characterization of synchrotron X-ray diffraction data with *ab initio* Maximum Entropy Method analysis reveals Mg^{2+} insertion into octahedral sites within the large vdW space between [V$_4$Se$_{18}$]$_\infty$ chains. Fast rate performance is attributed to low structural perturbation and low diffusion barriers, calculated by bond valence pathway analysis, resulting from the low charge-per-size of anionic selenium. X-ray photoelectron spectroscopy and X-ray absorption spectroscopy reveal that reversible insertion of Mg^{2+} is facilitated by V^{5+}/V^{3+} redox. V$_2$Se$_9$ demonstrates that selenides, despite their larger molecular weight, offer potential as fast-rate positive electrode materials for magnesium batteries over well-explored oxides and sulfides.

Introduction

Performance limitations, safety concerns, and the availability of the necessary raw materials for rechargeable Li-ion batteries have created a demand for innovative energy storage technologies beyond lithium.[1,2] The high natural abundance, low cost and high volumetric capacity of magnesium (3833 mA h cm^{-3}) compared to that of lithium (2046 mA h cm^{-3}) and sodium (1125 mA h cm^{-3}) make rechargeable Mg batteries an appealing alternative.[3–6]

The most significant challenge preventing the commercialization of magnesium batteries is a lack of suitable positive electrode materials capable of suitable kinetics for Mg^{2+} insertion. Despite the comparable ionic radii of Mg^{2+} and Li$^+$ (0.57 *vs.* 0.59 Å),[7] the high charge density of Mg^{2+} results in strong electrostatic interaction between the anionic sub-structure of the host electrode and the inserting ion.[8,9] As a result, Mg-

[a]Department of Chemistry, University of Liverpool, Liverpool, L69 7ZD, UK. E-mail: hardwick@liverpool.ac.uk; M.J.Rosseinsky@liverpool.ac.uk

[b]Stephenson Institute for Renewable Energy, Liverpool L69 7ZF, UK

[c]Materials Research Laboratory, Materials Department, University of California, Santa Barbara, California, CA 93106, USA

[d]Albert Crewe Centre, University of Liverpool, Research Technology Building, Elisabeth Street, Pembroke Place, Liverpool, L69 3GE, UK

[e]Johnson Matthey Technology Centre, Sonning Common, Reading, RG4 9NH, UK

[f]School of Physical Sciences, University of Kent, Canterbury, CT2 7NH, UK

[g]School of Engineering, Department of Mechanical, Materials and Aerospace Engineering, University of Liverpool, Liverpool, L69 7ZD, UK

† Electronic supplementary information (ESI) available. See DOI: https://doi.org/10.1039/d4ta04469j

storage is hindered both thermodynamically, with limited reaction reversibility; and kinetically, with sluggish Mg^{2+} insertion into the host structure.[10]

Increasing the polarizability of the anion framework has resulted in improved kinetic performance of insertion electrodes: layered VSe$_2$ and TiSe$_2$ demonstrate faster Mg^{2+} migration than the isostructural sulfide and oxide materials, albeit at a lower working potential.[11–17] Similarly, capacity retention has been improved in well-studied electrode materials like the Chevrel phase Mo$_6$S$_{8-x}$Se$_x$ $(0 < x \leq 2)$[18,19] and CuS$_{1-x}$Se$_x$ $(0 < x \leq 0.25)$[20–22] by partial substitution of S for Se. The enhanced kinetics of Mg^{2+} storage following the trend of Se > S > O can be attributed to both weakening electrostatic interactions as well as increasing anionic radii resulting in larger channels for Mg^{2+} diffusion.[23]

Recently, one-dimensional chain materials like VS$_4$,[24–27] V$_2$PS$_{10}$,[28] and TiS$_3$ (ref. 29 and 30) have attracted interest as positive electrode materials for Mg batteries. Their structures are comprised of one-dimensional chains formed from *trans*-facially connected [MS$_8$] polyhedra bound loosely by weak van der Waals (vdW) forces with large inter-chain spacing (5.38 Å in VS$_4$); through which Mg^{2+} can diffuse. These materials are noted for the complex insertion mechanisms, emanating from anionic redox on the disulfide (S$_2$)$^{2-}$ site.[31] The highly active anion chemistry of these materials provides motivation to explore S/Se substitution.

The structure of V$_2$Se$_9$, like VS$_4$ and V$_2$PS$_{10}$, consists of infinite one-dimensional chains of [V$_4$Se$_{18}$]$_\infty$ formed by *trans*-facial stacking of distorted rectangular anti-prismatic [VSe$_8$] polyhedra. These chains extend along the [302] direction and are weakly bound by vdW forces. The large anionic radius of Se

This journal is © The Royal Society of Chemistry 2024

J. Mater. Chem. A, 2024, **12**, 32349–32358 | **32349**

results in large inter-chain spacings of 6.366–6.610 Å for V_2Se_9, significantly longer than those observed in VS_4 and V_2PS_{10}. The oxidation states in V_2Se_9 can be considered by the asymmetric unit $V_2^{5+}(Se_2)^{2-}{}_4Se^{2-}$, where all Se are coordinated to a V^{5+} metal center and exist in either a $(Se_2)^{2-}$ or Se^{2-} oxidation state (a detailed structural description is provided in the ESI, Fig. S1 and Table S1†).

Recently, V_2Se_9 was investigated as an electrode material in monovalent Li^+ and Na^+ batteries and was shown to operate by a combination of insertion and conversion mechanisms.[32–34] Initially, up to nine Li^+ or Na^+ are inserted between the $[V_4Se_{18}]_\infty$ chains by an intercalation-type process. At lower potentials, conversion reactions result in the formation of metallic V and either Li_2Se or Na_2Se.

Herein, Mg^{2+} insertion into V_2Se_9 with fast kinetics is reported. Through detailed structural analysis of synchrotron X-ray diffraction (SXRD) data, combined with maximum entropy method analysis and bond valence diffusion pathway analysis, Mg^{2+} sites are located within the structure and highlight the inter-connected three-dimensional diffusion pathways and low structural perturbation as the origin of fast Mg^{2+} insertion. *Ex situ* X-ray photoelectron (XPS) and X-ray absorption spectroscopic (XAS) characterization and Raman spectroscopy were used to elucidate an insertion mechanism resulting from a reversible V^{5+}/V^{3+} redox couple, with no evidence of parasitic conversion reactions which were seen for Mg^{2+} insertion into VS_4.

Experimental section

V_2Se_9 synthesis

Powdered vanadium (99.5% Alfa Aesar) and selenium (99.5% Sigma Aldrich) were combined in stoichiometric quantities in an agate pestle and mortar in an inert Ar atmosphere in a glovebox (MBraun LabMaster 130; H_2O and O_2 levels < 0.1 ppm) before being pressed into pellets (13 mm diameter at 0.5 tonnes) and sealed in fused silica ampules under a vacuum of 1×10^{-5} mbar before heating to 623.15 K in a Carbolite RHF 1600 furnace for 21 days using heating and cooling rates of 5 K min^{-1} (Fig. S2 and Table S2†). After synthesis, the pellets were collected and homogenized by further grinding. Elemental analysis by ICP-OES yielded a composition of $V_{2.00(2)}Se_{9.4(3)}$ (Fig. S3 and Table S3†). TEM-EDX yielded a Se/V ratio of 4.31(18) (Fig. S4 and S5 and Table S4†). Further details for ICP-OES, TEM and TEM-EDX measurements is provided in the ESI.† Se and VSe_2 were observed as minor impurity phases by XRD in the as-made V_2Se_9 and the Mg-intercalated powders. The relative weight ratios of these impurity phases did not change between the pristine and intercalated materials.

Electrochemical cell assembly and testing

Stainless steel coin cells (CR2032, Pi-KEM) assembled under an inert Ar atmosphere inside a glovebox (MBraun LabMaster Pro-Eco) with O_2 and H_2O levels < 0.1 ppm. Positive electrodes consisted of a slurry of V_2Se_9 powder, sieved through a 20 μm mesh (Impact Test Systems), conductive carbon (Pi-KEM, dried), and binder (PVDF, dried) in proportions of 70 : 20 : 10

w/w combined with in *N*-methyl-2-pyrrolidone. The slurry was cast onto carbon-coated aluminium foil and cut into disks (16 mm diameter) and dried under vacuum overnight. Active material loadings were typically between 0.25 and 0.35 mg cm^{-2}, with an electrode thickness of 100 μm. Negative electrodes consisted of polished Mg foil discs with a diameter of 18 mm. Electrodes were separated by Whatman GF/D borosilicate glass fibre membranes soaked with 500–750 μL of an electrolyte consisting of a 0.5 M solution of magnesium bis(trifluoromethane)sulfonimide ($Mg(TFSI)_2$, 99.5%, Solvionic) dissolved in a mixture of dimethoxyethane (DME, Sigma Aldrich, anhydrous, inhibitor-free, 99.5%) and 1-methoxypropyl-2-amine (MPA, Sigma Aldrich, 99%) in a 3.84/1 w/w ratio (Fig. S6†).[35] The $Mg(TFSI)_2$ had been dried at 220 °C under a dynamic vacuum of ≈ 5 mbar for 12 h. DME was further dried over activated molecular sieves (Sigma Aldrich, 3 Å, heated to 250 °C under vacuum). MPA was degassed by freeze–pump–thaw with liquid N_2 and dried by distillation over CaH_2 before storing over activated molecular sieves. A final water content of <10 ppm was recorded by Karl-Fischer titration (Table S5†). Electrolyte stability was confirmed by cyclic voltammetry and Mg plating and stripping (Fig. S7 and S8†).

Electrochemical measurements were conducted using a Bio-Logic VSP300 potentiostat at 30 °C. Galvanostatic charge–discharge was performed between potential limits of 0.8–2.2 V *vs.* Mg^{2+}/Mg at current densities of 20–200 mA g^{-1}, recording the change in potential every 5 mV. *Ex situ* cell testing was performed on powder-based Swagelok cells. The cathode composition was 70% active material, 30% carbon black, without binder with typical loadings of 15–20 mg. Cells were discharged and charged with a constant current of 20 mA g^{-1} to the required potentials. Powders were collected, washed in DME, and dried under vacuum at 60 °C for 12 h.

Potentiostatic Intermittent Titration Technique (PITT) utilised chronoamperometric pulses imposed from open circuit potential to 0.8 V *vs.* Mg^{2+}/Mg with an interval of 20 mV until the current reach 0.75 mA g^{-1} at each potential step. Diffusion coefficients (D) were calculated by differentiation of the finite-diffusion Cottrell equation for the long-time region:

$$I = \frac{2nFAD\Delta C}{a}e^{\left(-\pi^2 Dt/a^2\right)}$$

where I is current (A), n number of transferred electrons, F Faraday constant (96 485 C mol^{-1}), A surface area (cm^2), ΔC for concentration gradient within the particles, t for time (s) and a for particle radius (cm).

X-ray diffraction (XRD) techniques

Synchrotron X-ray diffraction (SXRD) was performed at Diamond Light Source, U.K., on high-resolution beamline I11.[36,37] The patterns were recorded in the transmission mode [$0° < 2\theta < 90°$] using a position sensitive detector (PSD, $\lambda = 0.824399$ Å) at room temperature on samples introduced into 0.3 mm diameter borosilicate glass capillaries. Rietveld refinements were carried out using TOPAS Academic Version 7.[38] The background was fitted manually using a 36-part linear profile. Fundamental

32350 | *J. Mater. Chem. A*, 2024, **12**, 32349–32358

This journal is © The Royal Society of Chemistry 2024

parameters of the beamline were modelled, including Lorentz-polarization, *la, lo and lh* Voight coefficients, source-to-sample radius & slit widths. Peak profiles were fitted using the Stephens model in the monoclinic setting (*b*-axis unique). Simple axial model was initially constrained to 5.0 before being refined after initial peak profile fitting.

Maximum Entropy Method (MEM) was used to calculate electron density distributions. The observed structure factor was extracted from data using a Rietveld refinement performed in Jana 2006.[39] The refinement models were taken from Topas refinements and atomic positions were kept fixed. Peak profiles were fit empirically using a pseudo-Voight function and the Stephens model for anisotropic strain broadening in the monoclinic setting, as was done in Topas. The background was fit manually using a 60-point linear interpolation to ensure that peak intensities were extracted to the highest degree of accuracy. The electron densities were generated with MEM using the Sakata–Sato algorithm in BayMEM[40] on a grid of $300 \times 300 \times 300$ voxels and run till the combined FG constraint met its convergence criteria of 1.0. Electron densities were visualized using VESTA.[41]

Mg^{2+} diffusion pathways in V_2Se_9 were analyzed by bond valence pathway analysis (BVPA) using the software SoftBV GUI (Version 1.3.1).[42] Three-dimensional energy landscape maps were generated for Mg^{2+} ion diffusion using soft bond valence parameters calculated using the CIF generated from SXRD data for V_2Se_9. Maximum voxel resolution of 0.1 Å was applied. The resulting volumetric data was visualized using an isosurface level of 5.0 α_0^{-3} (α_0: Bohr radius) using the VESTA software.[41]

Elemental analysis

Scanning Transmission Electron Microscopy (STEM) imaging, and EDX analysis were performed using a Cs-corrected TEM/STEM Jeol 2100FCs microscope operating at 200 kV. For EDX mapping, a JEOL silicon drift detector (SDD) was used with a detection area of 100 mm^2.

Further details regarding Transmission Electron Microscopy (TEM) and Inductively Coupled Plasma Optical Emission Spectroscopy (ICP-OES) can be found in the ESI.†

Raman spectroscopy

Ex situ Raman measurements were collected using a Raman microscope (Renishaw, in *via* reflex coupled with an inverted Leica microscope), with a 532 nm laser as the excitation source (power <300 μW), focused onto the sample using *a* ×50 objective (Olympus). The collected Raman spectra were baseline-corrected. The spectral measurement time was 60 seconds with 5 accumulations to ensure a good signal-to-noise ratio and well-resolved peaks. To check for potential laser damage, V_2Se_9 was measured with varying laser intensities and exposure times. No changes in the spectra were observed up to 10% power for 60 seconds.

X-ray photoelectron and X-ray absorption analysis

X-ray Photoelectron Spectroscopy (XPS) analysis was performed using a Thermo NEXSA XPS fitted with a monochromatic Al Kα X-ray source (1486.7 eV), a spherical sector analyser and multichannel resistive plate, 128 channel delay line detectors. All data were recorded at 19.2 W with an X-ray beam size of 400 $\times$ 200 μm^2. Survey scans were recorded at a pass energy of 200 eV, and high-resolution scans were recorded at a pass energy of 40 eV. Electronic charge neutralization was achieved using a dual-beam low-energy electron/ion source (Thermo Scientific FG-03). The ion gun was operated at a current of 150 μA and a voltage of 45 V. All sample data were recorded at a pressure below 10^{-8} Torr and at 294 K. Data was processed using CasaXPS (v2.3.19PR1.0) using a Shirley background and peak fitting with Gaussian–Lorentzian functions. The Fermi edge of Ni foil measured using the same equipment was used to calibrate the data and eliminate any effects of surface charging.

X-ray Absorption Spectroscopy (XAS) was measured at beamline B18 (ref. 43) at Diamond Light Source, U.K. Pellets of sample diluted with cellulose were prepared with an optimized density for X-ray absorption measurements in transmission mode at the V K-edge (5465 eV) and the Se K-edge (12 658 eV) at ambient temperature. The samples were hermetically sealed in Al pouches under argon. The spectra were calibrated by fixing the maximum of the derivative of V and Se foil references placed after the samples for the corresponding edges, respectively, and normalized with the Athena software.[44]

Results and discussion

Cyclic voltammetry was used to probe the operational potential window and redox activity of V_2Se_9 towards electrochemical (de)insertion of Mg^{2+} in 0.5 M magnesium bis(trifluoromethane)sulfonimide $Mg(TFSI)_2$ in dimethoxyethane (DME) and 1-methoxy-2-propylamine (3.84 : 1 w/w) electrolyte (Fig. S6–S8 and Table S5†). From an open circuit potential (OCP) of 1.8 V *vs.* Mg^{2+}/Mg the cell potential was swept at a rate of 100 μV s^{-1} while the reductive potential was lowered, from 0.9 V to 0.2 V (Fig. 1a). When cycled between 0.8 V and 2.4 V, a sharp reductive peak is observed at 1.72 V, with additional weaker peaks observed at 1.36 V, 1.25 V and 1.13 V. Strong oxidative peaks are observed above 1.6 V, centered at 1.72 V and 1.95 V, though several smaller less resolved peaks are also present. The inflection at 2.4 V was shown to be oxidation of the electrolyte solution, which continued as the potential was further increased. This observation is similar to other reports which use $Mg(TFSI)_2$ electrolyte solutions in the literature and is in-line with the potential at which $[TFSI]^-$ has been shown to corrode Al in Li-ion based systems.[45,46] When the potential is swept below 0.6 V there is an almost immediate loss of redox activity, suggesting the system undergoes irreversible changes below *ca.* 0.7 V (Fig. S9†). Low-potential conversion reactions are observed in V_2Se_9 in Li^+ and Na^+ cells when cycled below 1.5 V *vs.* Li$^+$/Li (0.83 V *vs.* Mg^{2+}/Mg) and 1.0 V *vs.* Na$^+$/Na (0.66 V *vs.* Mg^{2+}/Mg).[32–34] Similar conversion reactions are likely occurring with Mg^{2+} at potentials below 0.7 V. This is indeed the case for structurally related one-dimensional chain materials containing sulfur, such as VS_4 and TiS_3, which display low-potential conversion reactions in which MgS and metallic V are formed.[47–49] While the formation of Li_2Se and Na_2Se is shown to
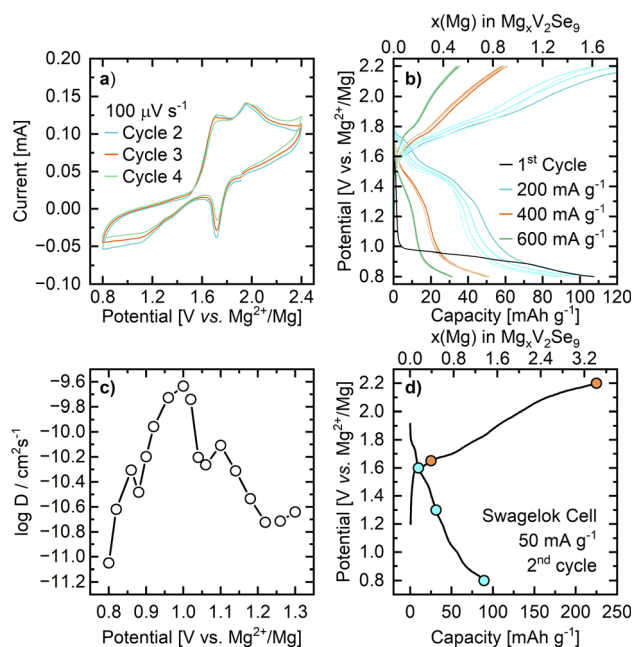
This journal is © The Royal Society of Chemistry 2024

J. Mater. Chem. A, 2024, **12**, 32349–32358 | **32351**

Fig. 1 (a) Cyclic voltammogram recorded for $Mg_xV_2Se_9$ at a sweep rate of 100 $\mu V\ s^{-1}$ between 0.8 V and 2.4 V. (b) Voltage profiles of cycles 1–12 for V_2Se_9 in 0.5 M $Mg(TFSI)_2$ in dimethoxyethane/1-methoxypropyl-2-amine (3.84/1, w/w) at 200–600 mA g^{-1}. (c) Potentiostatic intermittent titration technique of the discharge of V_2Se_9 to calculate the Mg^{2+} diffusion coefficients as a function of potential, from 1.3 V to 0.8 V. (d) Second cycle discharge potential profile for V_2Se_9/carbon loose powder electrode in a Swagelok cell at a current density of 50 mA g^{-1} for *ex situ* analysis. Spheres represent the potentials at which cells were stopped and the materials collected: cyan for discharged (magnesiated) $Mg_xV_2Se_9$ and orange for charged (de-magnesiated) $Mg_xV_2Se_9$. Typically, a second discharge capacity of 90 mA h g^{-1} (*i.e.*, 1.35 Mg^{2+}/V_2Se_9) is achieved by 0.8 V. Samples of $Mg_xV_2Se_9$ were collected at 1.6 V ($x = 0.15$); 1.3 V ($x = 0.47$); and 0.8 V ($x = 1.35$) during discharge; and 1.65 V ($x = 0.97$) and 2.2 V ($x = 0.00$) during charging.

be reversible, the formation of MgS is not, and results in significant capacity decay over the first few cycles. It is therefore reasonable to expect that the formation of MgSe is also irreversible. The large charge-per-size of Mg^{2+} compared to Li^+ and Na^+ will result in stronger Mg–Se bonding in MgSe than Li–Se and Na–Se bonds in Li_2Se and Na_2Se, respectively. As such, a suitable potential window of 0.8 V to 2.2 V was selected for galvanostatic cycling.

During the first cycle, an initial discharge capacity of 107 mA h g^{-1} is observed at a current density of 200 mA g^{-1}. The first cycle shows a different initial potential profile to subsequent cycles. The potential drops rapidly to 1 V, suggesting a large overpotential activation for Mg^{2+} insertion whereas upon further cycling, Mg begins to be inserted at a much higher potential of 1.6 V. Subsequent cycles achieve a decreasing amount of capacity from 106 to 88 mA h g^{-1} (*i.e.*, 1.6–1.3 Mg^{2+}/V_2Se_9) at 200 mA h g^{-1} with potential profiles remaining similar; with plateaus at 1.75 V, 1.50 V and 1.35 V (Fig. 1b), consistent with the peak positions observed in cyclic voltammetry. The capacity decreases at higher current densities, with 50 mA h g^{-1} (0.76 Mg^{2+}/V_2Se_9) at 400 mA g^{-1} and 31 mA h g^{-1}

(0.47 Mg^{2+}/V_2Se_9) at 600 mA g^{-1} being maintained for multiple cycles. This is lower than the capacity achieved by the insertion of Li^+ or Na^+ into V_2Se_9, which can be estimated to be 300 mA h g^{-1} from insertion reactions alone.[32,33] This can likely be attributed to the associated thermodynamic and kinetic difficulties with the insertion of high charge-per-size Mg^{2+} relative to Li^+ and Na^+.

Mg^{2+} de-insertion appears to be a more complex process with voltage hysteresis observed during charging. Plateaux are observed at 1.65 V, 1.72 V, and 1.85–1.90 V, again in agreement with peaks observed during cyclic voltammetry. An extended plateau is observed above 2.1 V that originates from the oxidation of the electrolyte as the potential approaches the upper limit of the electrochemical stability window (Fig. S8†), accounting for the larger capacity observed on charging.[50] As a result, this difference in capacity is observed for cycles at slower rates, with higher current densities achieving higher coulombic efficiencies (Fig. S10†).
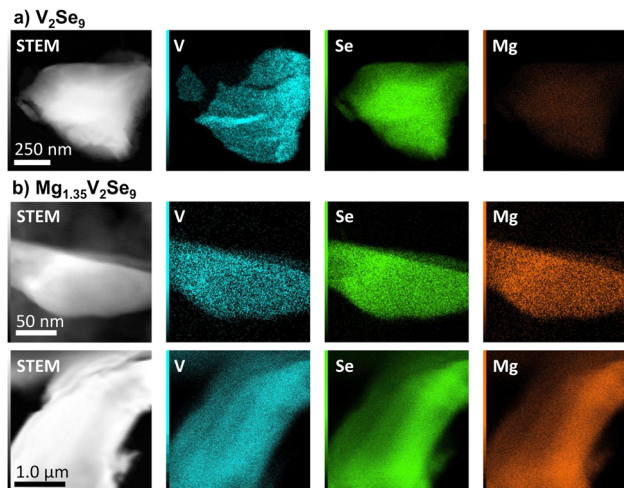
Magnesium insertion diffusion was studied using Potentiostatic Intermittent Titration Technique (PITT); the calculated diffusion coefficients from the selected points are illustrated in Fig. 1c. The Mg^{2+} diffusion coefficients in $Mg_xV_2Se_9$ are $\approx 10^{-10}$–10^{-12} cm^2 s^{-1}, and change as a function of potential indicating Mg content-dependent insertion kinetics. The kinetic performance of V_2Se_9 towards Mg^{2+} insertion is faster than V_2PS_{10} (10^{-14}–10^{-11} cm^2 s^{-1} between 1.5 and 0.1 V)[28] and Mo_6S_8 (10^{-14}–10^{-11} cm^2 s^{-1} between 1.4–1.0 V);[18,51] and is comparable to monovalent charge carrier (Li^+, Na^+) insertion into layered oxide materials.[52,53] The observed rapid kinetics of V_2Se_9 can be attributed to the low-charge-density selenide framework, helping to overcome the sluggish kinetics of Mg batteries.

To understand the storage mechanism of V_2Se_9, Swagelok-type cells with cathodes consisting of approximately 20 mg of 70/30 w/w V_2Se_9/carbon black powder (no binder) were used to prepare samples of $Mg_xV_2Se_9$ for *ex situ* diffraction, XPS, and XAS measurements. Typically, a second discharge capacity of 90 mA h g^{-1} (*i.e.*, 1.35 Mg^{2+}/V_2Se_9 giving $Mg_{1.35}V_2Se_9$) is achieved by 0.8 V (Fig. 1d). The lower capacity is the result of reduced conductivity between the loose powder electrode in Swagelok cells compared to cast electrodes in coin cells. The long plateau above 2.1 V is attributed to electrolyte oxidation, as previously discussed.

STEM-EDX false color micrographs shown in Fig. 2 confirm that Mg is homogeneously distributed throughout the bulk of V_2Se_9 crystallites after insertion. ICP-OES analysis gives a composition of $Mg_{1.20(3)}V_{2.00(8)}Se_{9.4(5)}$, in good agreement with the expected Mg content from the electrochemical discharge capacity (Table S6†). *Ex situ* SXRD analysis was performed on $Mg_xV_2Se_9$ ($0 \leq x \leq 1.35$) prepared at various potentials during discharge: 1.6 V ($x = 0.15$); 1.3 V ($x = 0.47$); 0.8 V ($x = 1.35$); and recharge: 1.65 V ($x = 0.97$) and 2.2 V ($x = 0.00$).

Analysis of SXRD data for $Mg_{1.35}V_2Se_9$ (discharged to 0.8 V *vs.* Mg^{2+}/Mg) indicates that the structural symmetry ($C2/c$) and framework of V_2Se_9 is retained for cycled $Mg_xV_2Se_9$ (Fig. 3a). Fourier difference analysis reveals two separate regions of electron density as suitable positions for Mg^{2+} within the unit

32352 | *J. Mater. Chem. A*, 2024, **12**, 32349–32358

This journal is © The Royal Society of Chemistry 2024

Fig. 2 STEM dark field and false color EDX micrographs of (a) V_2Se_9 (b) and $Mg_{1.35}V_2Se_9$ (after discharge to 0.8 V; shown in for separate areas) using an acceleration voltage of 200 kV with a probe current of 7.475 nA. V is shown in blue, Se in green and Mg in orange. The Mg content cannot be resolved due to overlap between the Mg K_a (1.253 keV) and Se L_a (1.379 keV) peaks. Mg signal is within the limits of noise in V_2Se_9. For $Mg_{1.35}V_2Se_9$ Mg is homogeneously inserted throughout the crystallite.

cell (Fig. 3b and c and S11†). Magnesium was placed on each of these sites with an initial occupancy of 1.0 (equivalent to $Mg_2V_2Se_9$) before refinement. The proximity of magnesium positions to V and Se sites was restrained using a penalty function during final refinement, and the B_{iso} values for both Mg sites were constrained to be equal. The final structural model (shown in Fig. 3a) achieved fit statistics of $R_{wp} = 0.521\%$, improved from 0.624% for a model without any Mg present (Fig. S12 and Table S7†).

The location of the two refined Mg positions is further confirmed through analysis of the SXRD data *via* maximum entropy method (MEM) calculations by generating the electron density distribution *ab initio* from the observed diffraction data.[40] Analysis was performed on both pristine V_2Se_9 and $Mg_{1.35}V_2Se_9$ to visualize the change in charge density upon reduction of the host structure. Fig. 3d and e shows electron density observed between neighboring $[V_4Se_{18}]_\infty$ chains of $Mg_{1.35}V_2Se_9$ which is not present in V_2Se_9, further confirming Mg is present on these sites (Fig. S13†). Notably, the electron density observed on the Mg sites is more localized than that of the larger, and therefore less densely charged, neighboring Se sites.

The refined occupancies of the two Mg sites were 0.596(19) and 0.402(16), providing a refined composition of $Mg_{0.99(3)}V_2Se_9$, compared to $Mg_{1.35}V_2Se_9$ calculated from electrochemical capacity. Identification of discrete Mg sites suggests a homogeneous distribution of Mg^{2+} within bulk V_2Se_9, indicative of an insertion-type electrochemical process. Additionally, no metallic V or MgSe is observed *via ex situ* diffraction measurements, suggesting that no conversion processes take place when cycling between 0.8–2.2 V.

Mg is octahedrally coordinated to Se in $Mg_{1.35}VSe_9$, with MgSe$_6$ octahedra located in the vdW space between neighboring
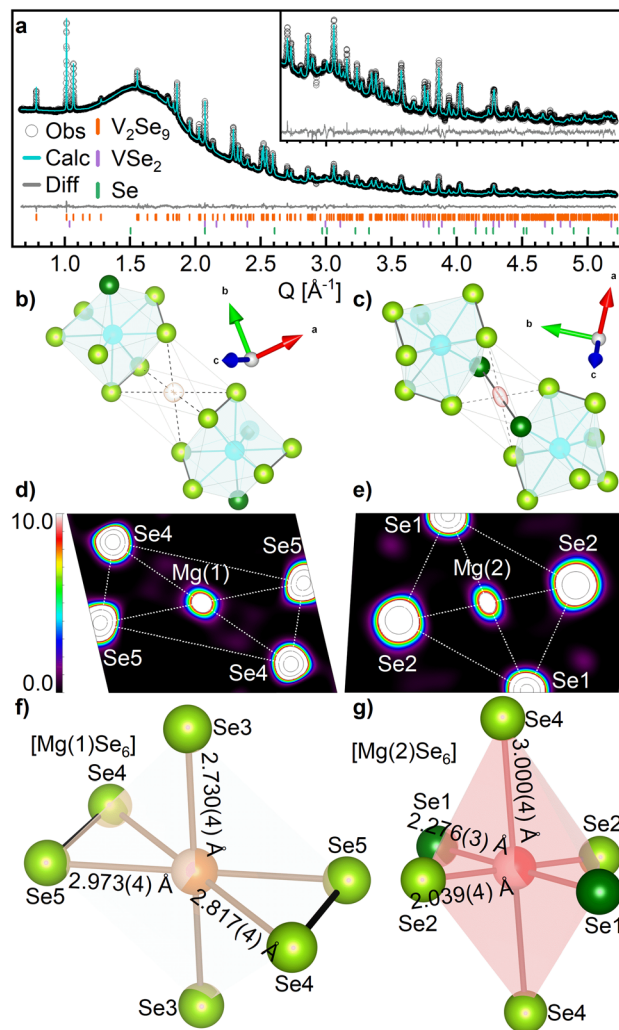
Fig. 3 (a) Rietveld refinement of $Mg_{1.35}V_2Se_9$ against SXRD data collected at I11 beamline. Observed data are shown by white circles. The calculated fit is shown by the cyan line. The difference between the calculated and observed data are shown by the grey line. The Bragg reflection positions of V_2Se_9, VSe_2 and Se are given by the orange, purple and green ticks, respectively. Inset is an enlarged region of the fit between 2.5–5.2 Å^{-1}. Refined parameters are summarized in Table S7.† (b–g) Coordination of Mg sites in $Mg_{1.35}V_2Se_9$. V is shown by blue spheres, Mg(1) by orange spheres, Mg(2) by red spheres, Se^{2-} by dark green spheres and Se^{1-} by light green spheres. Se–Se bonds are shown by bold black lines and V–Se and Mg–Se bonds are shown by grey lines. Electron density isosurfaces of the Mg(1) and Mg(2) sites in $Mg_{1.35}V_2Se_9$ generated by (b and c) Fourier difference analysis and (d and e) maximum entropy method. 2D planes bisect the MgSe$_6$ octahedrons in the equatorial plane (see Fig. S13†). (f and g) Local coordination environments of Mg(1) and Mg(2).

$[V_4Se_{18}]_\infty$ chains. Selenide materials containing octahedral MgSe$_6$ units involving Se^{2-} only, such as spinel MgM$_2$Se$_4$ (M = In, Al, Sc),[54] olivine Mg$_2$MSe$_4$ (M = Ge, Si, Sn)[55] and Mg$_2$P$_2$Se$_6$ (ref. 56) have average Mg–Se distances of 2.74(9) Å with a range of 2.3–3.3 Å (Fig. S14†), and average polyhedral volumes of 27.2(4) Å^3. In $Mg_{1.35}V_2Se_9$, Mg(1) is coordinated entirely to Se^{1-} anions with an average Mg–Se distance of 2.84(12) Å and an octahedral volume of 21.51 Å^3 (Fig. 3f). Mg(2) is coordinated to

This journal is © The Royal Society of Chemistry 2024

J. Mater. Chem. A, 2024, **12**, 32349–32358 | **32353**

four Se^{1-} and two Se^{2-} anions with an average Mg–Se distance of 2.4(5) Å and an octahedral volume of 17.85 Å^3 (Fig. 3g). The smaller Mg(2) octahedra is attributed to a lower Mg occupancy and the smaller anionic radius of Se^{2-}. Additionally, the mixed coordination of Mg(2) to Se^{1-} and Se^{2-} results in a larger octahedral distortion index than that of Mg(1) (0.154 compared to 0.031) due to different anionic radii and charge densities.[57]

Each VSe_8 polyhedron shares faces with two $MgSe_6$ octahedra, with one Mg(1) and one Mg(2); likewise, each $MgSe_6$ octahedron shares two opposite, and identical, faces with two separate VSe_8 polyhedra from neighboring $[V_4Se_{18}]_\infty$ chains. Every $(Se_2)^{2-}$ group is coordinated to at least one Mg^{2+} site. Mg(1) shares two triangular faces with VSe_8 formed between $Se(1)^{2-}$, $Se(2)^{1-}$ and $Se(4)^{2-}$. Mg(2) shares two triangular faces formed between $Se(3)^{1-}$, $Se(4)^{1-}$, and $Se(5)^{2-}$, such that two edges of Mg(2) Se_8 octahedron is formed by the $(Se_2)^{2-}$ bond between Se(4) and Se(5) (Fig. 4a). In this way, chains of $[V_4Se_{18}]_\infty$ that are separated by vdW gaps in V_2Se_9 are connected in $Mg_{1.35}V_2Se_9$ through Se–Mg–Se bonds (Fig. 4b).

The structural model for $Mg_{1.35}V_2Se_9$ was used as a starting model for refinement against SXRD data for other *ex situ* samples of $Mg_xV_2Se_9$ after discharging ($0 \le x \le 1.35$): 1.6 V ($x = 0.15$); 1.3 V ($x = 0.47$); 0.8 V ($x = 1.35$); and after charging: 1.65 V ($x = 0.97$) and 2.2 V ($x = 0.00$). Refined Rietveld parameters and fits are given in Fig. S15 and Tables S8–S11.†

Refinement of Mg site occupancies shows Mg content in $Mg_xV_2Se_9$ increases as potential is decreased (Fig. S16a†). After discharging from the OCV (1.8 V) to 1.6 V the occupancy of Mg(1) increases to 0.227(17), while Mg(2) is only 0.061(17). Mg(1) occupancy continues to increase rapidly to 0.553(14) by 1.3 V and more slowly to 0.596(11) by 0.8 V; suggesting that Mg(1) is filled more easily in the earlier stages of electrochemical discharge, as would be expected given the larger octahedral volume and low charge density Se^{1-} coordination of this site. The occupancy of Mg(2) increases to 0.263(14) by 1.3 V and 0.402(12) by 0.8 and is therefore filled more easily in the later stages of discharge, but to a lesser degree than Mg(1). This supports the measured PITT data (Fig. 1c), which shows faster kinetics in the early stages of Mg insertion before decreasing later in the discharge process. The preferential occupation of Mg(1) over Mg(2) is likely attributed to favorable kinetics associated with the interaction of high-charge density Mg^{2+} with the lower charge density Se^{1-} (to which Mg(1) has a higher coordination) compared to Se^{2-}. None of the Mg sites observed through *ex situ* structural analysis are fully occupied and, likely, the higher capacities recorded for non-*ex situ* cells (Fig. 1b and d) are the result of greater occupancy of these sites with increased Mg insertion due to the difference in cell preparation. Upon charging from 0.8 to 2.2 V, refinement shows that magnesium is de-intercalated from $Mg_{1.35}V_2Se_9$, reforming V_2Se_9.

To better understand the facile Mg^{2+} insertion kinetics observed by PITT, Mg^{2+} ion conduction pathway energy landscapes were calculated from soft bond valence parameters by bond valence pathway analysis (BVPA) (further details are given in the ESI†).[58] 2D and 2D Mg^{2+} diffusion pathways are observed

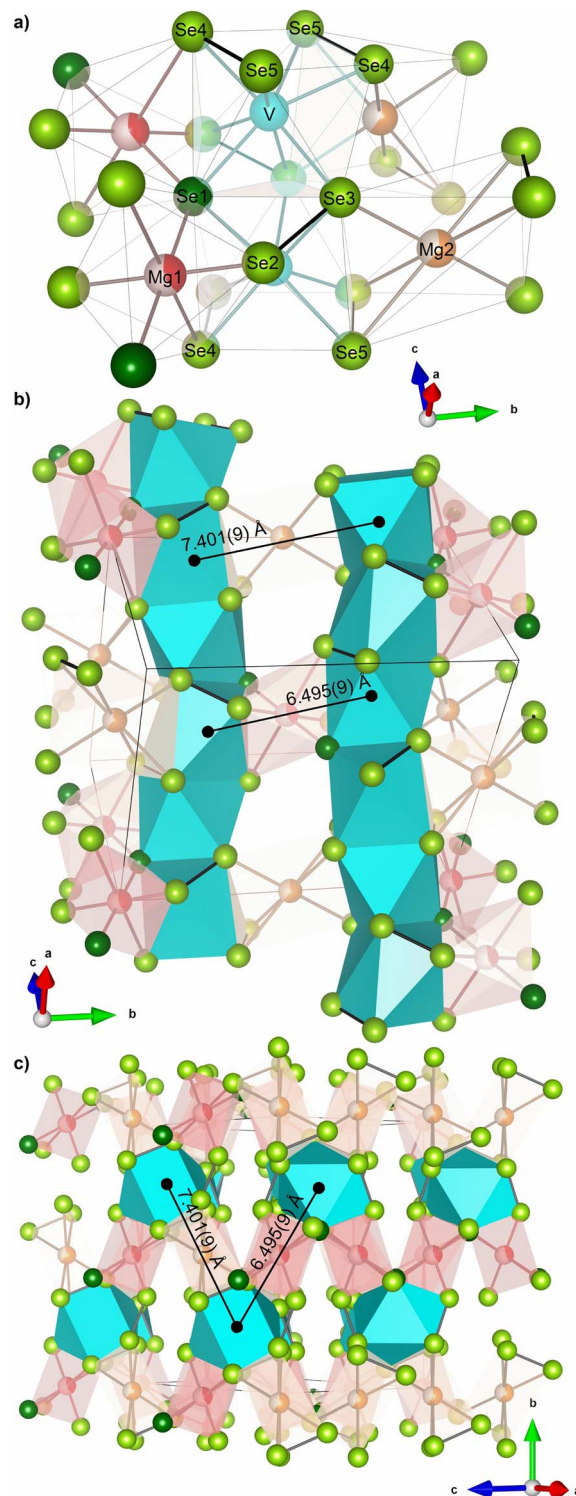Fig. 4 The structure of $Mg_{1.35}V_2Se_9$. V is shown by blue spheres, Mg(1) by orange spheres, Mg(2) by red spheres, Se^{2-} by dark green spheres and Se^{1-} by light green spheres. Se–Se bonds are shown by bold black lines and V–Se and Mg–Se bonds are shown by grey lines. (a) The coordination of Mg sites around V_2Se_9. (b and c) Chains of $[V_4Se_{18}]_\infty$ that are separated by vdW space in V_2Se_9 are connected through Se–Mg–Se bonding in $Mg_{1.35}V_2Se_9$ in the (011) plane. V–V interchain distances across Mg sites are provided.

32354 | *J. Mater. Chem. A*, 2024, **12**, 32349–32358

This journal is © The Royal Society of Chemistry 2024

in V_2Se_9, with energy barriers ranging from 0.140 to 0.742 eV (Fig. S17 and S18†).[44–46]

Locally, this results in minimal strain induced on the individual $[VSe_8]$ polyhedra, which is evidenced by minimal change to average V–Se and Se–Se distances between V_2Se_9 and $Mg_{1.35}V_2Se_9$ (2.57(5) Å to 2.55(4) Å for V–Se; and 2.716(12) Å to 2.728(18) Å for Se–Se, respectively). The relatively small changes in V–Se distances are in line with other vanadium chalcogenide materials after electrochemical insertion of Mg^{2+}: V–O distances in MgV_2O_5 increase by only 0.03 Å compared to V_2O_5 (1.49 Å to 1.52 Å)[59] and V–S distances in $Mg_{1.5}VS_4$ increase by only 0.04 Å compared to VS_4 (2.40 Å to 2.44 Å).[25] The lower charge density of Se, compared to O and S, as well as the lower Mg/V ratio for $Mg_{1.35}V_2Se_9$ result in little to no change in the average V–Se bond length between V_2Se_9 and $Mg_{1.35}V_2Se_9$. The minimal change in Se–Se distances between V_2Se_9 and $Mg_{1.35}V_2Se_9$ indicates that $(Se_2)^{2-}$ bonds are maintained after Mg^{2+} insertion, unlike VS_4 (ref. 25) and V_2PS_{10} (ref. 28) where S–S bonds break upon discharge (increasing in length by up to 15%). A full comparison of bond lengths for V_2Se_9 and $Mg_xV_2Se_9$ ($0 \leq x \leq 1.35$) is provided in Table S12.†

More significant structural perturbation is observed in the relative positions of the $[V_4Se_{18}]_\infty$ chains across the vdW space, which are influenced by the location of the Mg sites. The V–V interchain distances between vanadium sites adjacent to Mg(1) increase by 0.1% (from 7.394(9) Å in V_2Se_9 Å to 7.401(9) Å) in $Mg_{1.35}V_2Se_9$ (Fig. 4b and c). This is different to the V–V interchain distances between vanadium adjacent to the lesser occupied Mg(2) site contract by 2% (from 6.625(10) Å to 6.495(9) Å). This suggests that at low levels of Mg^{2+} occupancy, the selenium anionic framework of the $[V_4Se_{18}]_\infty$ chains are attracted towards the high charge density intercalated ion. For $x(Mg) = 1.35$ in $Mg_{1.35}V_2Se_9$, this attractive force dominates, and the distance between $[V_4Se_{18}]_\infty$ chains decreases in all directions (Fig. S16b†).[25,28,59] The shortest inter-chain Se–Se distances decrease from 3.443(6) to 3.419(7) Å for $Se_1–Se_2$ and from 3.521(4) Å to 3.419 Å for $Se_2–Se_5$. This leads to contraction of the a, b, and c lattice parameters, each with an approximately equal induced strain of 0.1%, resulting in a 0.3% decrease in unit cell volume from 1063.225(19) Å^3 in V_2Se_9 to 1059.511(18) Å^3 in $Mg_{1.35}V_2Se_9$ (Fig. S16c†). After charging, the unit cell returns to 1062.988(13) Å^3, with lattice parameters close to that of V_2Se_9.

Spectroscopic methods were used to further examine the changes in the electronic structure of V_2Se_9 upon Mg insertion. Both V_2Se_9 and $Mg_{1.35}V_2Se_9$ crystalize in $C2/c$ symmetry (crystal class $2/m$). Group-theory analysis identifies 33 Raman active modes for V_2Se_9. V and 4 of the Se sites that make up the $(Se_2)^{2-}$ groups occupy 8f Wyckoff positions, each with 3 A_g and 3 B_g active modes, while Se^{2-} occupies a 4e site with 1 A_g and 2 B_g active modes (Tables S13–S15†).[60,61] Low structural symmetry results in overlapping modes and produces the convoluted spectra observed for V_2Se_9 in Fig. 5a. Similarly to Raman spectra of isostructural Nb_2Se_9 (ref. 62) and related VS_4,[47] the spectrum can be divided into two regions; with phonons in the low-wavenumber range, between 105 and 175 cm^{-1}, assigned to V–V and V–Se bending and stretching modes, and a high-
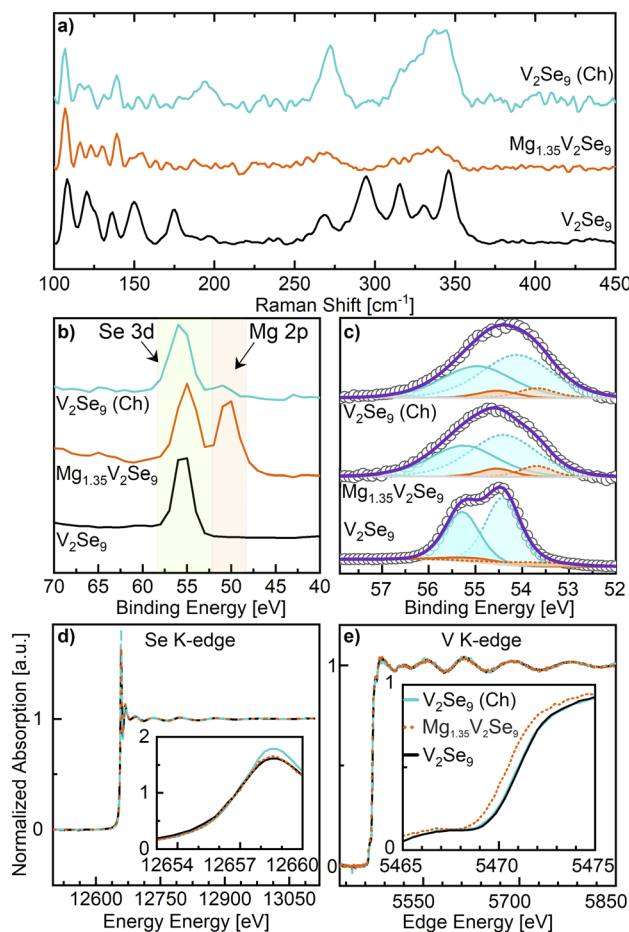

Fig. 5 (a) *Ex situ* Raman spectroscopy of V_2Se_9 (black), $Mg_{1.35}VSe_9$ (orange) after discharging to 0.8 V and V_2Se_9 after charging (Ch) to 2.2 V (cyan). (b and c) XPS spectra of $Mg_xV_2Se_9$ collected at various stages of discharge/charge. (b) Mg 2p collected at a pass energy of 200 eV and scaled using the Se 3d signal. (c) Se 3d XPS collected at a pass energy of 40 eV. Both Se 3d5/2 and Se 3d3/2 contributions are shown for each Se species: $(Se_2)^{2-}$ (light blue) and Se^{2-} (orange). The sum of orbital contributions is shown as the purple envelope relative to the observed data (black circles). The Se 3d5/2 and 3d3/2 spin−orbit components of each oxidation state were constrained based on relative position, $\Delta = 0.86$ eV, and intensity ratio = 0.735. The relative areas of $Se^{2-}/(Se_2)^{2-}$ for V_2Se_9 were constrained at 1/8, to reflect the nominal formula $V_2^{5+}(Se_2)^{2-}_4Se^{2-}$. Normalized (d) Se K-edge and (e) V K-edge XANES data measured in transmission for V_2Se_9 (black), $Mg_{1.35}V_2Se_9$ (discharged 0.8 V, orange), and V_2Se_9 (charged 2.2 V, cyan). Inset panels show enlarged profile of the absorption edges at 12 658 eV and 5465 eV, respectively.

wavenumber range, between 268 and 346 cm^{-1} (relating to shorter chemical bonds), assigned to Se–Se stretching and twisting as Se cage-breathing (Table S16†).

Ex situ Raman spectra collected for $Mg_{1.35}V_2Se_9$ (Fig. 5a) contain similar 33 Raman active A_g and B_g modes as V_2Se_9 as the octahedrally coordinated Mg^{2+} occupies 4a and 4b Wyckoff positions and possess no Raman active modes (Table S15†). The decrease in the intensity of signals observed between 268 and 346 cm^{-1} is the result of electron delocalization away from $(Se_2)^{2-}$ towards the Raman inactive Mg site, to which all $(Se_2)^{2-}$ are coordinated, resulting in reduced polarizability, and

This journal is © The Royal Society of Chemistry 2024

J. Mater. Chem. A, 2024, **12**, 32349–32358 | **32355**

dampening of the Raman signal.[63] Additionally, coordination of $(Se_2)^{2-}$ to Mg^{2+}, as well as the presence of Mg sites between $[V_4Se_{18}]_\infty$ chains, will limit the movement of Se sites to stretching, twisting, and breathing, further decreasing signal intensity. After charging to 2.2 V intense peaks in the high-wavenumber range are recovered supporting Mg de-insertion from the bulk.

X-ray photoelectron spectroscopy (XPS) measurements show the formation of peaks at 1303.2 eV, 89.0 eV, and 49.8 eV in $Mg_{1.35}V_2Se_9$ after discharge that are not present in V_2Se_9. These signals relate to Mg 1s, Mg 2s, and Mg 2p core levels, respectively (Fig. S22†), and relate to Mg insertion after discharging to 0.8 V. The low energy of the Mg 2p signal corresponds to higher kinetic energy electrons and is capable of probing deeper than Mg 1s and Mg 2s, and as such suggests that Mg is present beyond the immediate surface in $Mg_{1.35}V_2Se_9$.[64] The intensities of the Mg peaks is much lower after charging to 2.2 V, supporting Mg de-insertion (Fig. 5b), with the slight Mg signal that remains likely being due to the presence of surface species, which would explain why this feature is more prominent for the more surface sensitive Mg 1s and Mg 2s cores than Mg 2p.[65]

The Se 3d XPS signals contain contributions from both Se^{2-} and $(Se_2)^{2-}$ oxidation states (Fig. 5c and S23†). In V_2Se_9, the binding energy of the Se^{2-} $3d_{5/2}$ signal is at 53.4 eV; comparable to other vanadium selenide materials containing Se^{2-}.[66–68] The higher oxidation state Se^{1-} $3d_{5/2}$ signal is at a higher binding energy of 54.4 eV due to the increased interaction between the photo-emitted electron and the ion core.[69] The $(Se_2)^{2-}$ $3d_{5/2}$ signal is maintained at 54.4 eV in both V_2Se_9 and $Mg_{1.35}V_2Se_9$. The Se^{2-} $3d_{5/2}$ shows a slight shift in $Mg_{1.35}V_2Se_9$ relative to V_2Se_9 (from 54.7 eV to 53.7 eV) though its position is maintained after charging to 2.2 V. This is indicative of slight irreversible structural change occurring upon initial discharging supported by the signal broadening observed for both 0.8 V and 2.2 V samples. The relative areas of the $Se^{2-}/(Se_2)^{2-}$ signals is maintained at close to 1/8 (as in V_2Se_9); suggesting that Se is redox inactive between 0.8–2.2 V for $x(Mg)$ $0 \leq x \leq 1.35$, in agreement with the structural analysis via SXRD.

X-ray Absorption Near-Edge Spectroscopy (XANES) measurements of Se and V K-edges were used to monitor changes in the oxidation state of bulk $Mg_xV_2Se_9$ at the various stages of electrochemical cycling. Similarly to the Se 3d XPS measurements, there is no change in Se edge position observed by XANES upon discharge or charge (Fig. 5d). An average Se oxidation state between −1.08 and −1.11 is maintained between V_2Se_9, $Mg_{1.35}V_2Se_9$, and after charging to V_2Se_9 indicating the redox inactivity of Se (Fig. S24†). This differs from VS_4 (ref. 25) and V_2PS_{10} (ref. 28) which show changing contributions from signals relating to S^{2-} and $(S_2)^{2-}$ as S–S bonds are broken and reformed. Se has a lower electronegativity compared to S, meaning Se^{2-} is less readily formed than S^{2-} or O^{2-} which may explain why V_2Se_9 is anionic redox-inactive. While reversible cleavage of $(Se_2)^{2-}$ has been observed in molecular systems,[70] in solid materials Se–Se bonding is almost certainly less prone to redox activity than S–S or O–O. Cleavage of $(Se_2)^{2-}$ bonding in $Mg_xV_2Se_9$ may be the cause of irreversible electrochemistry below 0.8 V. The V K-edge XANES edge position decreases from

5471.0 eV for V_2Se_9 to 5470.5 eV for $Mg_{1.35}V_2Se_9$ after discharge, indicating a reduction from V^{5+} (Fig. 5e). Insertion of 0.675 Mg^{2+} per V requires the reduction of V^{5+} to $V^{3.65+}$. Upon charging, the vanadium edge energy and absorption profile return to that of V_2Se_9 (5471.0 eV), suggesting reversible redox processes take place on the V site and are responsible for Mg intercalation.

Conclusions

V_2Se_9 is capable of storing up to 1.6 Mg^{2+} (106 mA h g^{-1}) within the vdW spaces between its constituent one-dimensional chains. Detailed structural characterization by SXRD and MEM supports homogeneous distribution of Mg^{2+} ions within V_2Se_9, supporting an insertion-type electrochemical process without the formation of metallic V or MgSe that would be associated with a conversion-type reaction. Insertion of Mg^{2+} is facilitated by reversible redox on the V site, while $(Se_2)^{2-}$ is not redox active over the achieved levels of discharge. The octahedral coordination of Mg^{2+} results in minimal strain on the $[VSe_8]$ polyhedra, allowing for small changes in bond distances during Mg insertion, resulting in V_2Se_9 displaying exceptional Mg^{2+} diffusion kinetics, with diffusion coefficients surpassing state-of-the-art cathode materials such as $Mg_2Mo_6S_8$. Calculated bond valence parameters support diffusion pathways with low energy barriers to ion mobility are available to inserting Mg^{2+}. The one-dimensional structure of V_2Se_9 combined with the low charge density of coordinating $(Se_2)^{2-}$ and Se^{2-} anions enables rapid access to Mg^{2+} sites which enhances kinetic performance. Despite the larger mass of Se relative to S, V_2Se_9 can achieve comparable capacity to high-performance sulfide materials like Mo_6S_8, whilst operating with faster diffusion kinetics, helping to overcome the kinetic limitations that have perpetually hindered Mg^{2+} electrodes. This work motivates further investigation of tuning the anion chemistry of the wide range of known low-dimensional transition metal chalcogenides to improve kinetic performance of multivalent electrodes.

Data availability

The data supporting this article have been included as part of the ESI.† Underlying data collected as part of this work is available via the University of Liverpool data repository at **https://datacat.liverpool.ac.uk/id/eprint/2676**. The CIF files for the structures of V_2Se_9 and $Mg_{1.35}V_2Se_9$ are deposited with CSD accession codes 2357643 and 2357642, respectively.

Author contributions

Matthew A. Wright: conceptualization, data curation, formal analysis, investigation, methodology, visualization, writing – original draft, writing – review & editing; Jungwoo Lim, Raul A. Pacheco Muino: formal analysis, investigation, visualization, data curation; Anna E. Krowitz, Cara J. Hawkins, Mounib Bahri: investigation; Luke M. Daniels, Ruiyong Chen, Luciana Gomes Chagas: conceptualization, supervision, writing – review & editing; James Cookson, Paul Collier, Alan V. Chadwick, Nigel D Browning: funding acquisition, resources; John B. Claridge:

32356 | J. Mater. Chem. A, 2024, 12, 32349–32358

This journal is © The Royal Society of Chemistry 2024

conceptualization, supervision; Laurence J. Hardwick, Matthew J. Rosseinsky: conceptualization, funding acquisition, supervision, writing – review & editing.

Conflicts of interest

There are no conflicts to declare.

Acknowledgements

References

1 M. Armand and J. M. Tarascon, *Nature*, 2001, **414**, 359–367.
2 M. Mao, T. Gao, S. Hou and C. Wang, *Chem. Soc. Rev.*, 2018, **47**, 8804–8841.
3 J. Heelan, E. Gratz, Z. Zheng, Q. Wang, M. Chen, D. Apelian and Y. Wang, *JOM*, 2016, **68**, 2632–2638.
4 R. Davidson, A. Verma, D. Santos, F. Hao, C. Fincher, S. Xiang, J. Van Buskirk, K. Xie, M. Pharr, P. P. Mukherjee and S. Banerjee, *ACS Energy Lett.*, 2019, **4**, 375–376.
5 E. Levi, Y. Gofer and D. Aurbach, *Chem. Mater.*, 2010, **22**, 860–868.
6 C. Ling, D. Banerjee and M. Matsui, *Electrochim. Acta*, 2012, **76**, 270–274.
7 R. D. Shannon, *Acta Crystallogr.*, 1976, **A32**, 751–767.
8 Y. Liang, H. Dong, D. Aurbach and Y. Yao, *Nat. Energy*, 2020, **5**, 646–656.
9 Z. Guo, S. Zhao, T. Li, D. Su, S. Guo and G. Wang, *Adv. Energy Mater.*, 2020, **10**, 1903591.
10 M. Mao, T. Gao, S. Hou and C. Wang, *Chem. Soc. Rev.*, 2018, **47**, 8804–8841.
11 Y. Liang, R. Feng, S. Yang, H. Ma, J. Liang and J. Chen, *Adv. Mater.*, 2011, **23**, 640–643.
12 X. Sun, P. Bonnick, V. Duffort, M. Liu, Z. Rong, K. A. Persson, G. Ceder and L. F. Nazar, *Energy Environ. Sci.*, 2016, **9**, 2273–2277.
13 M. Liu, A. Jain, Z. Rong, X. Qu, P. Canepa, R. Malik, G. Ceder and K. A. Persson, *Energy Environ. Sci.*, 2016, **9**, 3201–3209.
14 H. D. Yoo, Y. Liang, H. Dong, J. Lin, H. Wang, Y. Liu, L. Ma, T. Wu, Y. Li, Q. Ru, Y. Jing, Q. An, W. Zhou, J. Guo, J. Lu, S. T. Pantelides, X. Qian and Y. Yao, *Nat. Commun.*, 2017, **8**, 339.
15 X. Sun, P. Bonnick and L. F. Nazar, *ACS Energy Lett.*, 2016, **1**, 297–301.
16 Y. Gu, Y. Katsura, T. Yoshino, H. Takagi and K. Taniguchi, *Sci. Rep.*, 2015, **5**, 12486.
17 D. Tao and F. Xu, *Mater. Lett.*, 2021, **300**, 130221.
18 M. D. Levi, E. Lancri, E. Levi, H. Gizbar, Y. Gofer and D. Aurbach, *Solid State Ionics*, 2005, **176**, 1695–1699.
19 G. S. Suresh, M. D. Levi and D. Aurbach, *Electrochim. Acta*, 2008, **53**, 3889–3896.
20 C. Du, Z. Han, H. Peng, J. Tian, X. Yang, T. Xia, X. Ma, Y. Zhu and C. Cao, *J. Power Sources*, 2022, **546**, 231673.
21 D. Chen, Y. Zhang, X. Li, J. Shen, Z. Chen, S. Cao, T. Li and F. Xu, *Chem. Eng. J.*, 2020, **384**, 123235.
22 Y. Cao, Y. Zhu, C. Du, X. Yang, T. Xia, X. Ma and C. Cao, *ACS Nano*, 2022, **16**, 1578–1588.
23 M. Mao, X. Ji, S. Hou, T. Gao, F. Wang, L. Chen, X. Fan, J. Chen, J. Ma and C. Wang, *Chem. Mater.*, 2019, **31**, 3183–3191.
24 Z. Li, B. P. Vinayan, P. Jankowski, C. Njel, A. Roy, T. Vegge, J. Maibach, J. M. G. Lastra, M. Fichtner and Z. Zhao-Karger, *Angew. Chem., Int. Ed.*, 2020, **59**, 11483–11490.
25 S. Dey, J. Lee, S. Britto, J. M. Stratford, E. N. Keyzer, M. T. Dunstan, G. Cibin, S. J. Cassidy, M. Elgaml and C. P. Grey, *J. Am. Chem. Soc.*, 2020, **142**, 19588–19601.
26 E. D. Grayfer, E. M. Pazhetnov, M. N. Kozlova, S. B. Artemkina and V. E. Fedorov, *ChemSusChem*, 2017, **10**, 4805–4811.
27 Y. Wang, Z. Liu, C. Wang, X. Yi, R. Chen, L. Ma, Y. Hu, G. Zhu, T. Chen, Z. Tie, J. Ma, J. Liu and Z. Jin, *Adv. Mater.*, 2018, **30**, 1802563.
28 M. A. Wright, T. W. Surta, J. A. Evans, J. Lim, H. Jo, C. J. Hawkins, M. Bahri, L. M. Daniels, R. Chen, M. Zanella, L. G. Chagas, J. Cookson, P. Collier, G. Cibin, A. V. Chadwick, M. S. Dyer, N. D. Browning, J. B. Claridge, L. J. Hardwick and M. J. Rosseinsky, *Angew. Chem., Int. Ed.*, 2024, **63**, e202400837.
29 M. Arsentev, A. Missyul, A. V Petrov and M. Hammouri, *J. Phys. Chem. C*, 2017, **121**, 15509–15515.
30 K. Taniguchi, Y. Gu, Y. Katsura, T. Yoshino and H. Takagi, *Appl. Phys. Express*, 2016, **9**, 11801.
31 A. M. Abakumov, S. S. Fedotov, E. V. Antipov and J.-M. Tarascon, *Nat. Commun.*, 2020, **11**, 4976.
32 S. Oh, C. Woo, J. Ahn, T. Y. Kim, X. Dong, Y. Kim, K. H. Choi, S. Chae, X. Zhang, H.-S. Bang, J. Kang, J. Jeon, H.-S. Oh, W.-S. Yoon, H. K. Yu and J.-Y. Choi, *ACS Appl. Mater. Interfaces*, 2023, **15**, 55745–55752.
33 S. Hwang, S. Oh, W. Choi, S. Chae, J. Ahn, W. Lee, H.-S. Oh, J.-Y. Choi and W.-S. Yoon, *J. Alloys Compd.*, 2024, **980**, 173541.
34 L. Liu, S. Xu, F. Tang, M. Wu, W. Yang, C. Xu and X. Rui, *Chem. Commun.*, 2023, **59**, 11365–11368.
35 S. Hou, X. Ji, K. Gaskell, P.-F. Wang, L. Wang, J. Xu, R. Sun, O. Borodin and C. Wang, *Science*, 2021, **374**, 172–178.
36 N. Tartoni, S. P. Thompson, C. C. Tang, B. L. Willis, G. E. Derbyshire, A. G. Wright, S. C. Jaye, J. M. Homer, J. D. Pizzey and A. M. T. Bell, *J. Synchrotron Radiat.*, 2007, **15**, 43–49.
37 S. P. Thompson, J. E. Parker, J. Potter, T. P. Hill, A. Birt, T. M. Cobb, F. Yuan and C. C. Tang, *Rev. Sci. Instrum.*, 2009, **80**, 75107.

This journal is © The Royal Society of Chemistry 2024

J. Mater. Chem. A, 2024, **12**, 32349–32358 | **32357**

38 A. A. Coelho, *J. Appl. Crystallogr.*, 2000, **33**, 899–908.

39 V. Petříček, M. Dušek and L. Palatinus, *Z. Kristallogr.–Cryst. Mater.*, 2014, **229**, 345–352.

40 S. van Smaalen, L. Palatinus and M. Schneider, *Acta Crystallogr., Sect. A: Found. Crystallogr.*, 2003, **59**, 459–469.

41 K. Momma and F. Izumi, *J. Appl. Crystallogr.*, 2011, **44**, 1272–1276.

42 L. L. Wong, K. C. Phuah, R. Dai, H. Chen, W. S. Chew and S. Adams, *Chem. Mater.*, 2021, **33**, 625–641.

43 A. J. Dent, G. Cibin, S. Ramos, A. D. Smith, S. M. Scott, L. Varandas, M. R. Pearson, N. A. Krumpa, C. P. Jones and P. E. Robbins, *J. Phys.: Conf. Ser.*, 2009, **190**, 12039.

44 B. Ravel and M. Newville, *J. Synchrotron Radiat.*, 2005, **12**, 537–541.

45 A. Abouimrane, J. Ding and I. J. Davidson, *J. Power Sources*, 2009, **189**, 693–696.

46 I. Shterenberg, M. Salama, H. D. Yoo, Y. Gofer, J.-B. Park, Y.-K. Sun and D. Aurbach, *J. Electrochem. Soc.*, 2015, **162**, A7118.

47 Y. Wang, Z. Liu, C. Wang, X. Yi, R. Chen, L. Ma, Y. Hu, G. Zhu, T. Chen, Z. Tie, J. Ma, J. Liu and Z. Jin, *Adv. Mater.*, 2018, **30**, 1802563.

48 S. Dey, J. Lee, S. Britto, J. M. Stratford, E. N. Keyzer, M. T. Dunstan, G. Cibin, S. J. Cassidy, M. Elgaml and C. P. Grey, *J. Am. Chem. Soc.*, 2020, **142**, 19588–19601.

49 K. Taniguchi, Y. Gu, Y. Katsura, T. Yoshino and H. Takagi, *Appl. Phys. Express*, 2016, **9**, 11801.

50 S. Hou, X. Ji, K. Gaskell, P.-F. Wang, L. Wang, J. Xu, R. Sun, O. Borodin and C. Wang, *Science*, 2021, **374**, 172–178.

51 E. Lancry, E. Levi, Y. Gofer, M. D. Levi and D. Aurbach, *J. Solid State Electrochem.*, 2005, **9**, 259–266.

52 N. Phattharasupakun, M. M. E. Cormier, E. Lyle, E. Zsoldos, A. Liu, C. Geng, Y. Liu, H. Li, M. Sawangphruk and J. R. Dahn, *J. Electrochem. Soc.*, 2021, **168**, 90535.

53 S. G. Lim, M. S. Kwon, T. Kim, H. Kim, S. Lee, J. Lim, H. Kim and K. T. Lee, *ACS Appl. Mater. Interfaces*, 2022, **14**, 33129.

54 P. Dotzel, H. Schäfer and G. Schön, *Z. Anorg. Allg. Chem.*, 1976, **426**, 260–268.

55 K. Wu, X. Su, Z. Yang and S. Pan, *Dalton Trans.*, 2015, **44**, 19856–19864.

56 W. Klingen, G. Eulenberger and H. Hahn, *Sci. Nat.*, 1968, **55**, 229–230.

57 J. Glinnemann, H. E. King Jr, H. Schulz, Th. Hahn, S. J. La Placa and F. Dacol, *Z. Kristallogr.*, 1992, **198**, 177–212.

58 L. L. Wong, K. C. Phuah, R. Dai, H. Chen, W. S. Chew and S. Adams, *Chem. Mater.*, 2021, **33**, 625–641.

59 Y. Xu, X. Deng, Q. Li, G. Zhang, F. Xiong, S. Tan, Q. Wei, J. Lu, J. Li, Q. An and L. Mai, *Chem*, 2019, **5**, 1194–1209.

60 G. F. Koster, J. O. Dimmock and R. G. Wheeler, *The Properties of the Thirty-Two Point Groups*, The MIT Press, Cambridge, 1963.

61 S. L. Altmann and P. Herzig, *Point-group Theory Tables*, Clarendon Press, Oxford, 1994, 704.

62 J. Lee, B. J. Kim, Y. K. Chung, W. G. Lee, I. J. Choi, S. Chae, S. Oh, J. M. Kim, J. Y. Choi and J. Huh, *J. Raman Spectrosc.*, 2020, **51**, 1100–1107.

63 Y. Matsuda, N. Kuwata, T. Okawa, A. Dorai, O. Kamishima and J. Kawamura, *Solid State Ionics*, 2019, **335**, 7–14.

64 J. F. Watts and J. Wolstenholme, *An Introduction to Surface Analysis by XPS and AES*, John Wiley & Sons, 2019.

65 C. Du, W. Younas, Z. Wang, X. Yang, E. Meng, L. Wang, J. Huang, X. Ma, Y. Zhu and C. Cao, *J. Mater. Chem. A*, 2021, **9**, 3648–3656.

66 T. G. Ulusoy Ghobadi, B. Patil, F. Karadas, A. K. Okyay and E. Yilmaz, *ACS Omega*, 2017, **2**, 8319–8329.

67 S. Chae, C. Woo, G. H. Gu, T. Y. Kim, J. Jeon, H. J. Kwon, S. Oh, K. H. Choi, X. Dong, J. Ahn, G. Asghar, H.-S. Oh, H. K. Yu, H. W. Kim and J.-Y. Choi, *ACS Appl. Nano Mater.*, 2023, **6**, 16242–16252.

68 K.-Y. Hwa, A. Ganguly, A. Santhan and T. S. Kanna Sharma, *Chemosphere*, 2021, **282**, 130874.

69 J. F. Moulder, W. F. Stickle, P. E. Sobol and K. D. Bomben, *Handbook of X-Ray Photoelectron Spectroscopy*, Perkin-Elmer, 1981, vol. 3.

70 X. Wang, S. Zhang, X. Wang, Y. Su, Y. Qiu and Z. Zhang, *Nat. Commun.*, 2014, **5**, 1–7.

32358 | *J. Mater. Chem. A*, 2024, **12**, 32349–32358

This journal is © The Royal Society of Chemistry 2024